Fragmentation of faceted crystalline wires

Nan Wang and Alain Karma

Phys. Rev. Materials **6**, 106002 — Published 7 October 2022

DOI: 10.1103/PhysRevMaterials.6.106002

Fragmentation of faceted crystalline wires

Nan Wang[1,2,3,4] and Alain Karma[2]
[1]*Department of Materials Science and Engineering, Guangdong Technion - Israel Institute of Technology, Shantou, Guangdong 515063, China*
[2]*Physics Department and Center for Interdisciplinary Research on Complex Systems, Northeastern University, Boston, MA 02115, USA*
[3]*Guangdong Provincial Key Laboratory of Materials and Technologies for Energy Conversion, Guangdong Technion - Israel Institute of Technology, Shantou, Guangdong 515063, China and*
[4]*Technion - Israel Institute of Technology, Haifa 32000, Israel*
(Dated: September 30, 2022)

The reduction of surface energy is a well-known driving force for the fragmentation of nanowires. Fragmentation can limit the service life of those small low-dimensional building blocks or can be controlled to induce beneficial shape changes. For an isotropic surface energy, fragmentation is analogous to the classic Rayleigh-Plateau instability of liquid jets. However, commonly synthesized crystalline nanowires have strongly anisotropic surface energies and exhibit facets coinciding with cusps in the Wulff plot. Depending on growth orientation, different fragmentation behaviors have been seen in nanowires. Using phase-field simulations, we show that fragmentation of faceted nanowires with cubic crystal symmetry may occur by a finite-amplitude nonlinear instability, as opposed to a Rayleigh-Plateau-like linear instability, depending on nanowire growth orientation. We carry out a weakly nonlinear analysis based on sharp interface theory to characterize the faceted nanowire shape corresponding to a surface-energy saddle point. The analysis predicts that the minimum amplitude of a periodic shape perturbation to trigger fragmentation increases with cusp strength but decreases inversely proportionally to the perturbation wavelength for long wavelength, in good quantitative agreement with phase-field predictions. The results provide the theoretical foundation to predict nanowire stability as a function of length and surface energy in diverse applications.

INTRODUCTION

Nanowires have been actively studied over the past few decades as potential building blocks for future electronic and energy conversion devices. Those low dimensional objects can be synthesized nowadays by a variety of bottom up approaches and numerous studies have been devoted to characterizing their electronic and mechanical properties. However, the morphological stability of nanowires has so far received less attention. Nanowires have been observed to fragment into particles during annealing, which activates surface diffusion and allows shape changes to occur on relatively short time scales [1–7]. Understanding this process is important since significant morphological evolution or fragmentation occurring on long time scales can potentially limit the service life of nanowire-based devices operating at moderate or elevated temperature. In addition, temperature-controlled morphological evolution offers an interesting avenue to induce beneficial shape changes of nanowires after synthesis, such as producing shape undulations that can enhance thermoelectric energy conversion efficiency [8, 9].

At the most basic level, nanowire fragmentation is driven by the reduction of surface energy and resembles the classic Rayleigh-Plateau (RP) instability that transforms a liquid jet into an array of droplets [10, 11]. This instability is linear in the usual sense that it occurs by amplification of perturbations of *arbitrarily small initial amplitude*. In the case of the capillary-driven RP instability, amplification occurs when the wavelength λ of spatially periodic perturbations of a liquid cylinder of radius R_0 exceeds a critical value $\lambda_c = 2\pi R_0$. Furthermore, the growth rate of the instability is maximum for a wavelength larger than λ_c that is also proportional to R_0 and sets the scale of the fragmentation process.

Unlike the surface energy of a liquid jet, the surface energy of a crystalline nanowire generally depends on the orientation of the surface with respect to a fixed reference set of crystal axes. The effect of this anisotropy on the RP instability has been investigated theoretically for the case where the nanowire surface is atomically rough and its energy γ is a smooth differentiable function of orientation [12–15]. For the simplest case depicted in Fig. 1 where the nanowire is assumed to be axisymmetrical (i.e. symmetrical about its central axis), orientation can be measured by the angle θ between the direction normal to the surface and a plane parallel to the central z axis of the nanowire coinciding with a crystal axis as illustrated in Fig. 1. Theory predicts [14] that the critical wavelength of the RP instability λ_c depends generally on the surface stiffness $\gamma + d^2\gamma/d\theta^2$ and can be much larger than $2\pi R_0$ for strong anisotropy ($d^2\gamma/d\theta^2 \gg \gamma$). This increase of λ_c reflects physically the stabilizing effect of anisotropy. For a surface normal corresponding to a minimum of γ for the unperturbed nanowire, anisotropy increases the energy cost of creating a surface undulation through the change of surface orientation, beyond the cost associated with the change of surface area that is already present for an isotropic surface energy. While this theory applies to differentiable forms of $\gamma(\theta)$, nanowires are typically faceted. Accordingly, $\gamma(\theta)$ generically exhibits a non-differentiable form

$$\gamma(\theta) = \gamma_f(1 + \delta|\theta - \theta_f| + \dots) \tag{1}$$

near facets that correspond to cusps in the surface γ-plot. This form stems physically from the fact that a vicinal surface near a facet at orientation θ_f is composed of steps with energy γ_s spaced a distance $d \approx h/|\theta - \theta_f|$ where h is the step height. The excess surface energy associated with step formation is

therefore given by Eq. (1) with $\delta = \gamma_s/(\gamma_f h)$. A true cusp of the form of Eq. (1) can be conceptualized as the limit of a rounded cusp that becomes infinitely sharp, which corresponds to the limit $d^2\gamma/d\theta^2 \to \infty$ where theory predicts that λ_c diverges. Hence, in this limit, a faceted nanowire is expected to be linearly stable against infinitesimal perturbations of arbitrarily large wavelength. This raises the basic question: How does a faceted nanowire fragment? Here we address this question using both computational and analytical approaches. We show that fragmentation can be induced by a finite amplitude perturbation and the minimum amplitude can be predicted analytically in a simple case as a function of the cusp strength δ and wavelength of the perturbation.

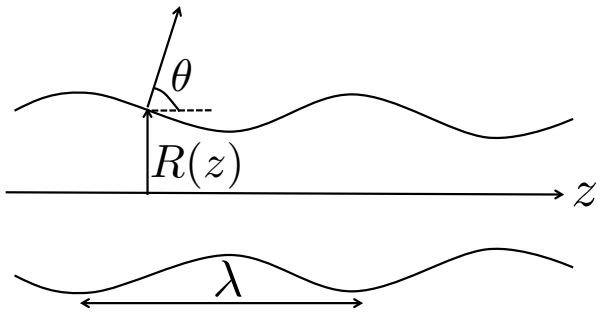

FIG. 1: Schematic representation of the longitudinal cross-section of a smoothly perturbed axisymmetrical nanowire, defining the angle θ between the direction normal to the surface and a plane parallel to the central z axis of the nanowire with $\cot\theta = -dR(z)/dz$ where $R(z)$ is the perpendicular distance from the z-axis to the surface.

The effect of a finite amplitude perturbation has been studied previously for an isotropic surface energy [16, 17], where fragmentation occurs by a RP instability for $\lambda > \lambda_c$. Those studies predict that, for $\lambda < \lambda_c$, fragmentation only occurs when the modulation amplitude exceeds a critical threshold $\sim \sqrt{\lambda_c - \lambda}$. This threshold stems physically from the fact that the nanowire shape needs to be perturbed beyond a critical shape that corresponds to a maximum energy saddle point for fragmentation to occur. For a faceted nanowire, λ_c is infinite such that the critical modulation amplitude is expected to be finite for arbitrarily large λ. Experimental observations of the morphological evolution of pore channels in sapphire [18–20] suggest that the breakup wavelength is reduced by introducing a finite amplitude perturbation. However, a quantitative understanding of the morphological stability of faceted nanowires under finite amplitude shape perturbations has remained lacking. The goal of the present study is to develop such an understanding by a combination of numerical and analytical calculations that focus on determining the saddle point nanowire shape in the presence of facets, from which we derive a relationship between the critical amplitude perturbation for fragmentation and the perturbation wavelength.

While our approach is general, we consider for concreteness a full three-dimensional (3D) anisotropic γ-plot with cubic symmetry of the form

$$\gamma(\hat{n}) = \gamma_0 \left[1 + \delta(|n^{100}| + |n^{010}| + |n^{001}|)\right], \qquad (2)$$

which is a function of local crystal surface normal $\hat{n}$, and n^{100}, n^{010} and n^{001} are the normal components along the corresponding crystal axes. The 3D equilibrium shape given by this γ has six $\{100\}$ facets connected by smoothly curved rough surfaces for other orientations. The size of $\{100\}$ facets relative to the rough parts increases with the parameter δ, which controls the magnitude of the cusps in the γ-plot at faceted orientations.

For the above form, the problem of computing the maximum energy saddle point for fragmentation of a nanowire is made highly non-trivial by the fact that the nanowire corresponding to this saddle point has a non-trivial 3D shape made up of flat facets connected by curved rough parts with different principal curvatures. For this reason, this fully 3D problem is solved here numerically by the phase-field (PF) method for nanowires oriented along $\{100\}$ (the $\{100\}$ direction aligns with the wire axial direction which is the z axis of the simulation box), $\{110\}$, and $\{111\}$. This problem, however, can be further simplified by assuming that the nanowire shape is axisymmetric, i.e. independent of azimuthal angle ρ in a cylindrical coordinate system (r, ρ, z) where z measures position along the central axis of the nanowire and $r = R(z)$ (Fig.1) is the radial distance to the surface perpendicularly to the z axis. In this approximation, the problem of computing the saddle point is reduced to finding a stationary nanowire shape $R(z)$ for an averaged surface energy over the perimeter arclength of the nanowire cross section that only depends on the angle θ defined in Fig. 1. We solve this axisymmetric problem both numerically and analytically in the long-wavelength limit for $\{100\}$ nanowires that, compared to $\{110\}$ and $\{111\}$ nanowires, turn out to be the most robust to perturbations for a γ-plot with $\{100\}$ facets described by Eq. 2. Our results demonstrate that the axisymmetric approximation predicts remarkably well quantitatively the critical perturbation amplitude required to fragment a fully 3D faceted nanowire. Furthermore, for the simple $\{100\}$ orientated nanowire, it allows us to compute analytically the saddle point shape in the large wavelength limit and to derive an explicit relationship between the critical perturbation amplitude and wavelength that agrees well with numerical solutions of the full non-axisymmetric 3D problem.

The article is organized as follows. The formulation of the 3D PF model for the nanowire fragmentation and its numerical results are presented in the next section. It is followed by the calculation of the averaged surface energy on the wire cross section, and the formulation of the axisymmetric model. An analytical theory based on the axisymmetric model is developed and compared with previous numerical results in section 4, followed by discussion and conclusions in section 5.

3D PHASE FIELD MODEL

PF models have been widely used in the study of materials microstructure evolution [21–24] covering many important research fields including ferroelectric materials [25, 26], 2 dimensional materials [27, 28], polycrystalline materials [29, 30], et al. This method conveniently incorporates the effect of surface energy in the evolution of micro/nano scale materials systems [31, 32]. Since the RP instability is a phenomenon driven by surface energy minimization, PF methods can be applied to study fragmentation behaviors related to the RP instability in various material systems.

A classical PF model uses a phase field parameter ϕ which takes distinct values in different phases and varies smoothly from one phase to another. For the fragmentation of nanowires, the PF parameter ϕ is set to be 1 in the wire and 0 everywhere-else. The PF model formulation is based on the following free energy functional

$$F = F_s - H\xi_{pf}\left[\int g(\phi)dv - V\right], \tag{3}$$

with the surface energy part

$$F_s = \int f_v(\phi)dv, \tag{4}$$

where the energy density $f_v(\phi)$ incorporates the anisotropic surface energy of the wire, H is a dimensional constant, dv is the volume element and the integration is over the entire simulation box. $g(\phi) = \phi^3(10 - 15\phi + 6\phi^2)$ is a monotonic function which equals 1 inside the wire and 0 outside. The total wire volume is conserved during the fragmentation process using the Lagrange multiplier ξ_{pf} which requires that the volume integral of $g(\phi)$ is equal to V at all time. Following previous PF model formulations with anisotropic surface energy, the energy density is written as

$$f_v(\phi) = H\left[\frac{w(\hat{n})^2}{2}|\nabla\phi|^2 + f_p(\phi)\right], \tag{5}$$

with

$$w(\hat{n}) = W\beta(\hat{n}), \tag{6}$$

$$f_p(\phi) = \phi^2(1-\phi)^2, \tag{7}$$

$$\hat{n} = -\nabla\phi/|\nabla\phi|, \tag{8}$$

where W is another dimensional constant with unit of length, and β is an anisotropy function. Integration of $f_v(\phi)$ across the interface region (from $\phi = 0$ to 1) gives the anisotropic surface energy in the model

$$\gamma(\hat{n}) = \gamma_0\beta(\hat{n}), \tag{9}$$

with $\gamma_0 = WH\sqrt{2}/6$.

In the RP instability theory, the evolution of the surface is the result of the competition between 2 principal curvatures. In the PF model, this is captured by deriving the equation of motion of the PF parameter ϕ from the variational principle

$$\begin{aligned} -\tau\frac{\partial\phi}{\partial t} &= \frac{1}{H}\frac{\delta F}{\delta\phi} \\ &= \frac{\partial f_p(\phi)}{\partial\phi} - \xi_{pf}\frac{\partial g(\phi)}{\partial\phi} - \sum_i\left\{\frac{\partial}{\partial x_i}[w(\hat{n})^2\phi_{x_i}]\right. \\ &\quad \left. + \frac{\partial}{\partial x_i}\left[|\nabla\phi|^2 w(\hat{n})\frac{\partial w}{\partial\phi_{x_i}}\right]\right\}, \end{aligned} \tag{10}$$

with spatial coordinate x_i $(i = 1, 2, 3)$, $\phi_{x_i} = \partial\phi/\partial x_i$. τ is a relaxation time constant. The Lagrange multiplier is

$$\xi_{pf} = \frac{\int \frac{dg(\phi)}{d\phi}\frac{\delta F_s}{\delta\phi}dv}{H\int\left[\frac{dg(\phi)}{d\phi}\right]^2 dv}, \tag{11}$$

which is derived by writing the volume conservation condition as

$$\frac{d}{dt}\int g dv = \int\frac{dg}{dt}dv = \int\frac{dg}{d\phi}\frac{d\phi}{dt}dv = 0, \tag{12}$$

and replacing $d\phi/dt$ using Eq.10. This volume conserving PF method is used to avoid slow surface diffusion dynamics which is given by $\frac{\partial\phi}{\partial t} = \nabla^2\frac{\delta F_s}{\delta\phi}$. The saddle point configuration we investigated in this work is only determined by the surface shape and is independent of the evolution dynamics.

Numerical implementation of Eq.10 is based on a finite difference scheme with spatial discretization $\Delta x/W = 0.4$ and Euler forward time integration. A cylindrical wire with an axisymmetric sinusoidal shape perturbation in the z-direction is used as the initial condition. The initial nanowire surface is given by $R(z) = R_0 + \frac{d}{2}\cos(2\pi z/\lambda)$ where $d = R_{max} - R_{min}$ is the surface modulation amplitude and λ is the perturbation wavelength, z is the coordinate along the wire axial direction. With $\phi = 1$ inside the wire and $\phi = 0$ outside, the contour surface $\phi = 0.5$ is used to mark the nanowire surface explicitly. The surface energy given in Eq.9 needs to be regularized in the numerical implementation. The regularization technique is described in appendix. The periodic boundary condition is applied along the z direction of the simulation domain. A single perturbation wavelength is included in the simulation domain, and the wire length under the periodic boundary condition becomes an integer times the simulation domain size. Dirichlet boundary conditions with $\phi = 0$ were imposed along the x and y directions

In the classic RP problem, a wire becomes unstable for any infinitesimal perturbation with the wavelength longer than the critical wavelength $\lambda_{c0} = 2\pi R_0$, where R_0 is the radius of the cylindrical wire. It is also found that, for the wavelength shorter than λ_{c0}, a finite amplitude perturbation is needed to

break the wire [16]. Analytically, this critical modulation amplitude can be obtained using weakly non-linear analysis based on an axisymmetric model without considering crystal surface anisotropy [16]. The reliability of the PF model is examined by finding the critical surface modulation amplitude d^* beyond which the finite amplitude perturbation with the wavelength shorter than the critical wavelength $\lambda_{c0} = 2\pi R_0$ will develop in Fig.2.

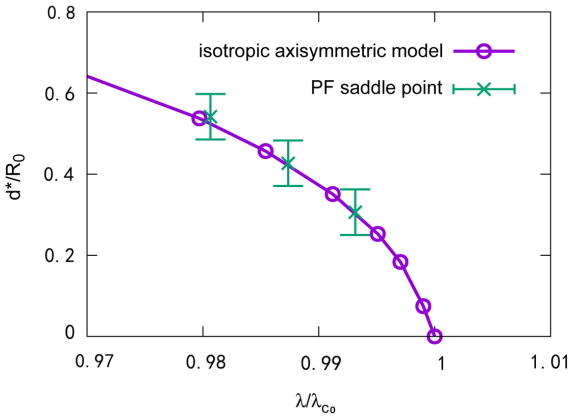

FIG. 2: Comparison of the critical modulation amplitude from the 3D PF model and the axisymmetric model for wires with isotropic surface energy. The 1D numerics points are obtained from the axisymmetric model with the nonlinear Newton solver described in appendix . The PF simulation results are obtained from initial conditions with slightly modified modulation amplitudes from the solutions of the axisymmetric model. Error bars in the PF results are marked by the initial modulation amplitude that breaks the wire (upper limit) or recovers the wire (lower limit). The axisymmetric model used here is discussed in later sections.

The PF model is then used to investigate the fragmentation condition for nanowires. The full cubic surface energy with various anisotropy strength δ and wire axial orientations are examined in the simulations. To connect with the isotropic RP problem, the critical wavelength λ_c is still used here by defining $\lambda_c = 2\pi R_0$ with R_0 being the radius of a uniform cylindrical wire with the same volume. The simulated surface evolution of $\{100\}$ oriented nanowires under finite amplitude perturbation is shown in Fig.3.

In Fig.3(a), the nanowire recovers from an initial finite amplitude shape perturbation gradually. In Fig.3(b), the 3D faceted wire shape and its evolution is demonstrated. With a slightly larger initial perturbation amplitude, Fig.3(c) shows a sequence of nanowire fragmentation. The critical saddle point surface configuration lies in the middle of the second snapshot of Fig.3(b) and 3(c). The critical modulation amplitude d^* decreases with increasing perturbation wavelength as shown in Fig.3(d) and 3(e).

The numerical study is then extended to $\{110\}$ and $\{111\}$ oriented nanowires. Without shape modulations, the cross sections of the $\{110\}$ and the $\{111\}$ wires closely match the equilibrium crystal shapes given by the corresponding anisotropic energy function perpendicular to the wire orientation as shown in Fig.4(b) and (c). Although energy cusps still appear on the sidewall orientation of those wires (Fig.4(d)), it is important to notice that these sidewalls on the $\{110\}$ and the $\{111\}$ nanowires are not all global energy minima in the anisotropic surface energy plot as they are in the $\{100\}$ oriented wires.

PF results of the critical modulation amplitude for the $\{110\}$ oriented wires are shown in Fig.4(e). From the comparison with the stabilizing effect in the $\{100\}$ oriented wires, one can see that the stabilizing effect of the energy cusps is drastically reduced in the $\{110\}$ case. For the $\{111\}$ oriented nanowire, the stabilizing effect is not observed in the PF simulations. This suggests that the $\{111\}$ oriented nanowires are subject to RP-type instability from infinitesimal perturbation beyond the critical wavelength λ_c.

While the surface energy regularization technique described in the appendix is used in the PF simulations, its effect on the results above is small and can be evaluated using the analytical theory in Ref.[12–14]. It has been shown in Ref.[14] that, with an axisymmetric form of the surface energy anisotropy, the critical wavelength is proportional to the square root of the surface stiffness $(\gamma + d^2\gamma/d\theta^2)$. Therefore, the critical wavelength diverges in the limit of sharp cusp independent of the type of regularization that is used. For the specific choice corresponding to equation 46, the stiffness diverges as δ/ϵ where ϵ is the small regularization parameter introduced in the equation, such that the critical wavelength of instability diverges in the small ϵ limit. For the full 3D anisotropy, we applied the theory in Ref.[12, 13] to the regularized surface energy in this work (Eq.45) and found that the critical wavelength in this case is proportional $\lambda_c/\sqrt{\epsilon}$ where λ_c is the critical wavelength for the isotropic case. For a small regularization parameter ϵ, the critical wavelength becomes much larger than the wire radius R_0 and the results of PF simulations that explore how fragmentation is induced by a finite amplitude perturbation which is measured by d/R_0 are ostensibly independent of ϵ. Therefore those results can be quantitatively compared to the prediction of the sharp-interface theory for a sharp cusp that is independent of ϵ.

The length in the PF model is scaled by the model parameter W related to both the surface width and the surface energy as in most PF models. For the PF model to be a good approximation to the problem, the W parameter should be chosen such that $W/R_0 << 1$. All the PF model parameters can then be decided with a given surface energy as indicated in Eq.9. Also, the current model is based on a given surface energy at a given temperature and is not meant to study the temperature dependence of the surface energy. In the case where the temperature varies during the experiment, one may introduce an interpolation of surface energies at different temperatures in the model.

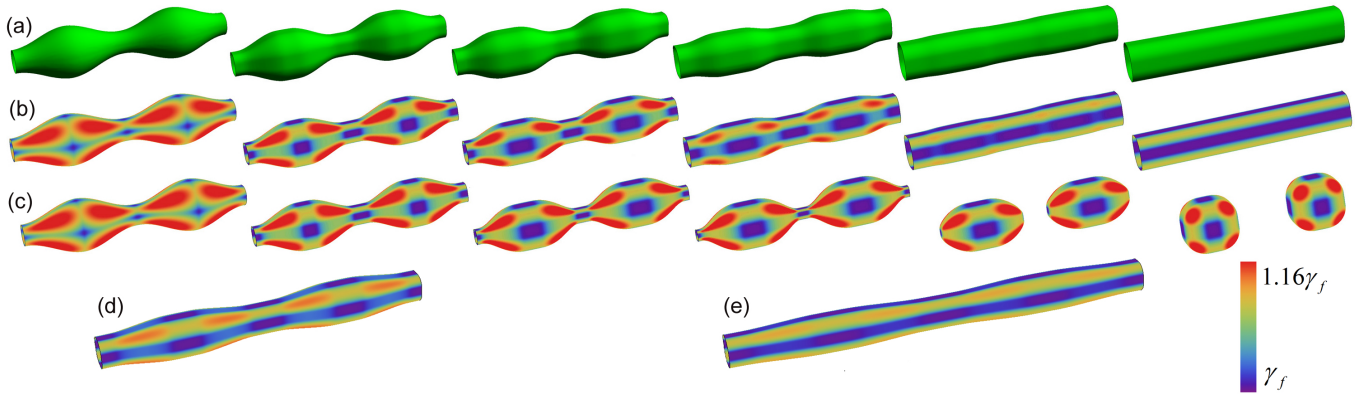

FIG. 3: (a) Recovery of a nanowire from shape perturbation. Time sequence goes from the left to the right. (b) The same recovery sequence in (a) but colored by local surface energy. (c) Fragmentation of the nanowire colored by local surface energy. The perturbation wavelength is $\lambda = \lambda_c$ in (a), (b) and (c). (d) The near-saddle surface configuration for $\lambda = 1.5\lambda_c$. (e) The near-saddle surface configuration for $\lambda = 2.0\lambda_c$. Cusp strength $\delta = 0.3$, γ_f in the colorbar is the surface energy of the faceted part given by $\gamma_0(1+\delta)$ in Eq.2.

AXISYMMETRIC MODEL

The demonstrated finite amplitude nanowire fragmentation results from the PF simulations in the previous section indicate that the fragmentation condition may have complex dependence on the 3D surface energy anisotropy, the perturbation wavelength and the wire orientation. In this section, an axisymmetric simplification to the 3D surface energy anisotropy is examined in details, and it is shown that this simplification can still captures the nanowire fragmentation condition rather well.

The first step to formulating an axisymmetric model is to map the nanowire to a cylindrical coordinate system (r, ρ, z) where the nanowire central axis coincides with the z axis. The low index crystal surface normals in the surface energy function Eq.2 can then be expressed using the inclination angle θ defined in Fig.1 and the azimuthal angle ρ in the cylindrical coordinate. For a $\{100\}$ oriented nanowire, the three crystal surface normals are $(n^{100}, n^{010}, n^{001}) = (\sin\theta\cos\rho, \sin\theta\sin\rho, \cos\theta)$. For $\{110\}$ and $\{111\}$ oriented nanowires, these crystal surface normals can be obtained through simple rotations as shown in appendix . To construct an axisymmetric model, one needs to come up with an effective average of the wire surface energy in the direction perpendicular to the wire axis. Two averaging approaches, azimuthal-angle average and arc-length average, are numerically examined.

The azimuthal average of the 3D surface energy anisotropy is

$$\gamma_{azi}(\theta) = \frac{1}{2\pi}\int \gamma(\theta,\rho)d\rho. \tag{13}$$

This average is calculated numerically for the $\{100\}$, $\{110\}$ and $\{111\}$ oriented nanowires in Fig.5(a). Near the side wall orientation where $\theta = \pi/2$, the γ_{azi} is shown in Fig.5(b). The surface energy cusp of γ_{azi} at $\theta = \pi/2$ in the $\{100\}$ oriented wires explains the enhanced stability under finite amplitude perturbations seen in the PF simulations, but the energy maximum for the $\{110\}$ oriented wires shown in the γ_{azi} plot is inconsistent with the weak stabilizing effect shown in the PF simulation results.

The arc-length average of the 3D surface energy anisotropy is

$$\gamma_{arc}(\theta) = \frac{\int \gamma(\theta,\rho)ds}{\int ds}, \tag{14}$$

where ds is the infinitesimal arc length on the wire surface. For a given θ, the 3D $\gamma(\theta,\rho)$ function is reduced to the 2D form $\Gamma(\rho)$ where it satisfies the anisotropic Gibbs-Thomson condition $\kappa[\Gamma(\rho) + \frac{d^2\Gamma}{d\rho^2}] = Const.$ with the local in-plane curvature $\kappa = d\rho/ds$. Using this relation, Eq.14 can be expressed as

$$\gamma_{arc}(\theta) = \frac{\int \gamma(\theta,\rho)[\Gamma(\rho) + \frac{d^2\Gamma}{d\rho^2}]d\rho}{\int[\Gamma(\rho) + \frac{d^2\Gamma}{d\rho^2}]d\rho}, \tag{15}$$

The numerical results of the arc-length average is shown in Fig.5(c) for orientations near the sidewall. While the stabilizing cusp in the $\{100\}$ case is very similar to the result in the azimuthal average, the $\{110\}$ case here has a small stabilizing cusp which is consistent with the PF simulations results. For the $\{111\}$ case, the arc-length averaged surface energy shows no stabilizing cusp which is also consistent with the PF simulation results. It is not surprising that the arc-length averaged result gives a better prediction to the wire stability comparing to the azimuthal-angle averaged result since the surface energy of the nanowire sidewall is $\int \gamma(\pi/2,\rho)ds$ where ds is the arc-length element along the sidewall perimeter, while the angular integral $\int \gamma(\pi/2,\rho)d\rho$ can only give a qualitatively

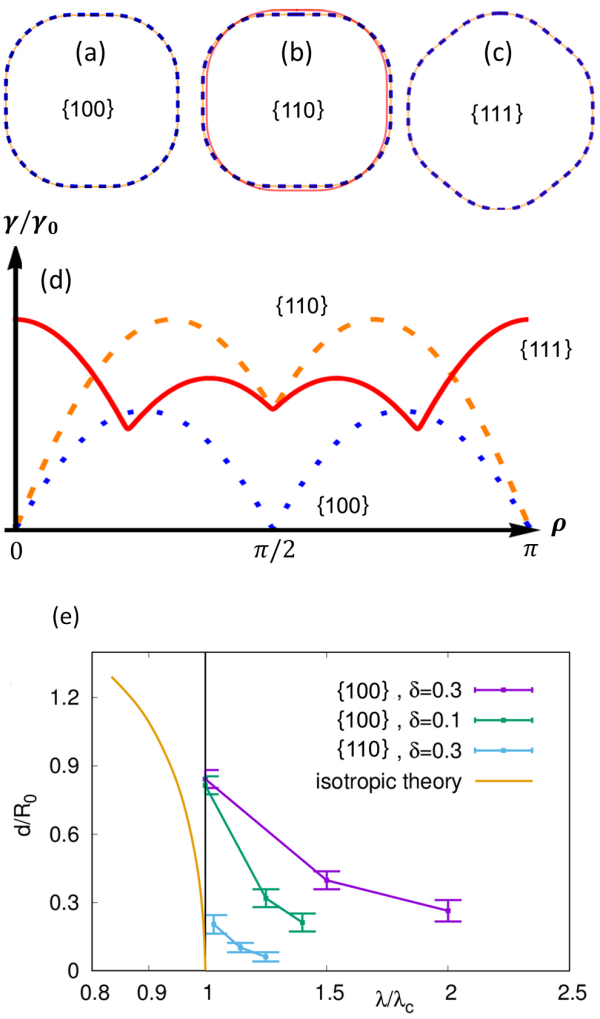

FIG. 4: (a-c) Equilibrium surface cross-sections for $\{100\}$, $\{110\}$ and $\{111\}$ oriented nanowires. Solid yellow line is from Wulff theory, blue dashed line is from PF numerical result. It is noted in panel (b) that the 4 facets in the $\{110\}$ cross section do not have equal length. To visualize the difference, A $\{100\}$ cross-section is included in panel (b) shown in solid red line. (d) Surface energy anisotropy function for the sidewall of $\{100\}$, $\{110\}$ and $\{111\}$ oriented nanowires. The plot range is limited to $(0, \pi)$. (e) Finite amplitude fragmentation condition for the $\{110\}$ oriented nanowires in comparison with the $\{100\}$ oriented wires.

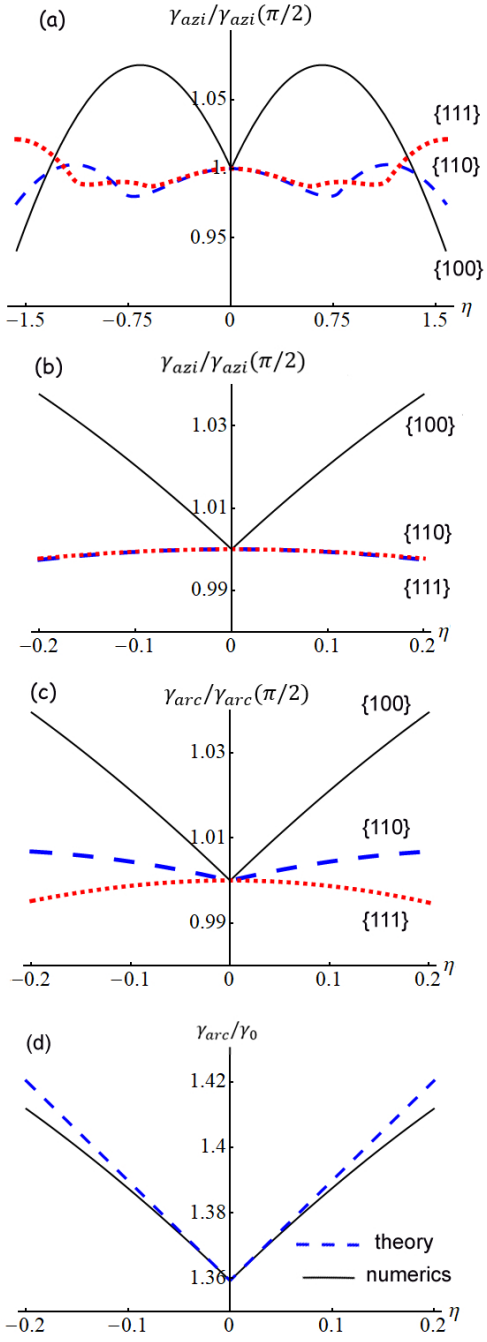

FIG. 5: Results from the azimuthal and the arc-length average of the surface energy. The x coordinate $\eta = \theta - \pi/2$. Anisotropy parameter $\delta = 0.3$. (a) The azimuthal average of the 3D surface energy for $\{100\}$, $\{110\}$ and $\{111\}$ oriented nanowires. (b) The near sidewall region of the azimuthal average shown in (a). (c) The near sidewall region of the arc-length average of surface energy. (d) Comparison of the numerically averaged surface energy using Eq.14 for the $\{100\}$ oriented wires with the theoretical result from Eq.21.

similar result when the curvature radius $R = ds/d\rho$ is a constant.

For the $\{100\}$ oriented nanowire, the arc-length averaged surface energy can also be calculated analytically as follows. The 3D surface energy function for the $\{100\}$ oriented wire is

$$\gamma = \gamma_0[1 + \delta(|\cos\theta| + |\sin\theta|(|\cos\rho| + |\sin\rho|))]. \quad (16)$$

The wire cross-section has 4 rough parts and 4 facets as shown in Fig.4. The total surface energy contribution from the rough parts is

$$F_r = 2\pi L_r \gamma_0 [1 + \delta|\cos\theta|] + 8R_0\delta\gamma_0|\sin\theta|, \quad (17)$$

where the azimuthal angle ρ has been integrated over 0 to 2π, and L_r is the curvature radius of the rough parts. The total surface energy contribution from the facets is

$$F_f = 8L_f\gamma_0[1 + \delta|\cos\theta|] + 8L_f\delta\gamma_0|\sin\theta|, \quad (18)$$

where L_f is a half of the facet length. The cross-section arc-length average of the γ function is then

$$\gamma_{arc}^{\{100\}}(\theta) = \frac{F_r + F_f}{2\pi L_r + 8L_f}. \quad (19)$$

Since the rough parts and the facets all satisfy the anisotropic Gibbs-Thomson condition $\kappa[\Gamma(\rho) + \frac{d^2\Gamma}{d\rho^2}] = Const.$, equating the averaged Gibbs-Thomson effect on a rough part with the averaged effect on a facet gives

$$\frac{\gamma_0}{L_r} = \frac{\int_{\frac{\pi}{2}-}^{\frac{\pi}{2}+} d(\frac{d\Gamma}{d\rho})}{2L_f}, \quad (20)$$

where the left hand side is obtained by averaging $\kappa[\Gamma(\rho) + \frac{d^2\Gamma}{d\rho^2}]$ over the rough part of the cross section and the average over the facet is $\int_{\frac{\pi}{2}-}^{\frac{\pi}{2}+} \kappa[\Gamma(\rho) + \frac{d^2\Gamma}{d\rho^2}]ds$ which can be simplified to the right hand side using $\kappa = d\rho/ds$. The equation above can be further reduced to $L_f = \delta L_r$ with the given surface energy for 100 oriented wires. The arc-length averaged surface energy is then simplified to

$$\gamma_{arc}^{\{100\}}(\theta) = \gamma_0[1 + \delta|\cos\theta| + \delta\frac{1+\delta}{\pi/4+\delta}|\sin\theta|] \quad (21)$$

This simple calculation assumes that the wire cross-section shape doesn't change significantly with θ which can only be true near the sidewall orientation $\theta = \pi/2$. The deviation of the Eq.21 from the numerical results is shown in Fig.5(d).

The $\gamma_{arc}(\theta)$ in Eq.21 is further adopted in the axisymmetric model, the surface energy in the axisymmetric model is then

$$F_s = 2\pi \int R\tilde{\gamma}\sqrt{1 + R_z^2}dz, \quad (22)$$

where $\tilde{\gamma} = \gamma_{arc}(\theta)$, R is the wire radius, R_z is the first derivative of R with respective to the axial coordinate z. Since there is no azimuthal variation of R in the axisymmetric model, R is only a function of z. The volume part of the free energy is $F_v = (\mu_{arc}/\Omega)\int \pi R^2 dz$ with the chemical potential of the wire atoms μ_{arc} and atomic volume Ω. Together, the total free energy is then $F = F_s + F_v$. Since the critical modulation saddle point in the axisymmetric model corresponds to a maximum energy configuration, it should satisfy the Euler-Lagrange equation

$$\frac{\delta F}{\delta R} = -\kappa_1\left(\tilde{\gamma} + \frac{d^2\tilde{\gamma}}{d\theta^2}\right) + \kappa_2\left(\tilde{\gamma} - R_z\frac{d\tilde{\gamma}}{d\theta}\right) - \frac{\mu_{arc}}{\Omega} = 0, \quad (23)$$

with two principle curvatures

$$\kappa_1 = -\frac{R_{zz}}{(1+R_z^2)^{3/2}}, \quad (24)$$

and

$$\kappa_2 = -\frac{1}{R(1+R_z^2)^{1/2}}, \quad (25)$$

where R_{zz} is the second derivative of R with respective to z. The κ_1 term is from the variation of R along the axial direction. The κ_2 term is from the cross-section curvature. With the knowledge of $\tilde{\gamma}$ from the analytical formula given previously, Eq.23 can be numerically solved with the nonlinear Newton solver discussed in Appendix .

For a given perturbation wavelength, there are two solutions of the nanowire surface shape, a trivial one that corresponds to a simple faceted nanowire, and a diameter modulated nanowire that corresponds to the maximum surface energy saddle point shape. Comparison of the axisymmetric model results with the PF results for the $\{100\}$ oriented wires is shown in Fig. 6.

Both the PF and the axisymmetric results exhibit significant stabilizing effects for $\lambda > \lambda_c$ as shown in Fig.6(a). The wire stability there depends on the relative modulation amplitude d/R_0. As λ becomes larger, the critical amplitude required to destabilize the nanowire becomes smaller. The surface variation of the saddle point configuration reaches a major fraction of the wire radius at short wavelength but decreases significantly as the perturbation wavelength increases in Fig.6(b). Nanowire shapes at the critical saddle point are shown in Fig. 6(c). Remarkably, the critical modulation amplitudes from the simple axisymmetric model match the 3D PF results fairly well.

WEAKLY NONLINEAR ANALYSIS

Since the axisymmetric model (Eq.23) captures the stabilizing effect of the sidewall facets rather well, further analytical work on the model may reveal the important relation between the wavelength-dependent stability condition and the anisotropic surface energy parameters. In the numerical solutions of the axisymmetric model in Fig.6(b), three different parts are shown on the modulated nanowire surface profile, two facets l_+ and l_- with different radius (upper and lower facets) and an intermediate rough part l_r connecting two facets as illustrated in Fig.7(a). Assuming the rough part can be constructed as a small (but finite) amplitude radial perturbation

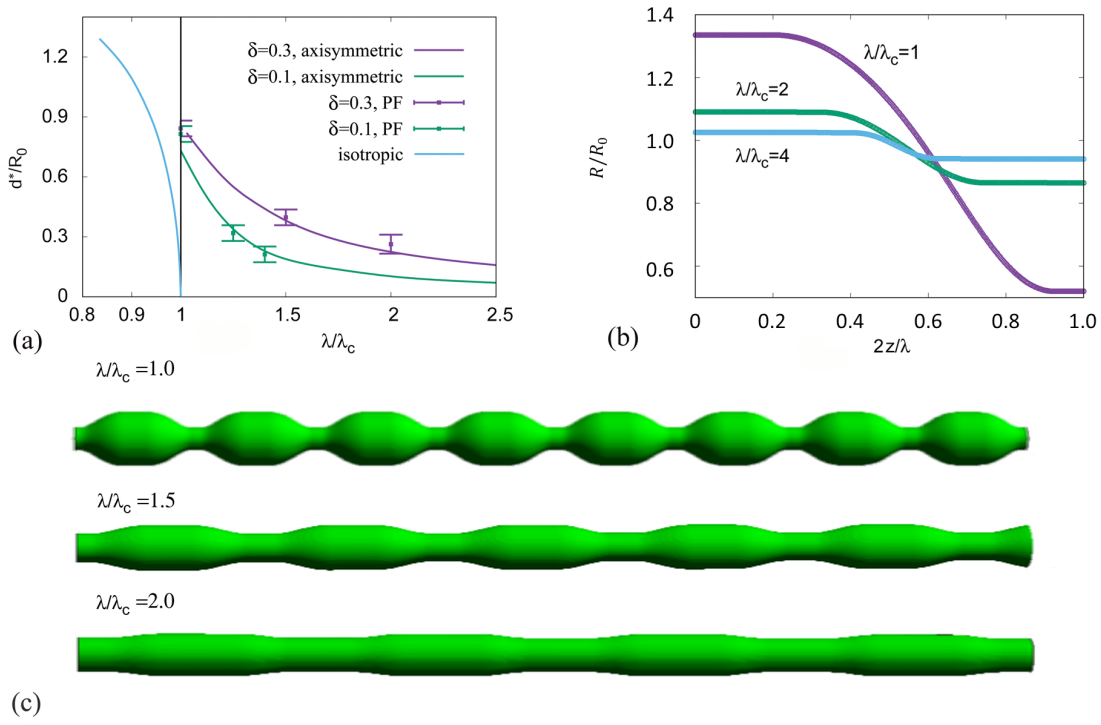

FIG. 6: (a) Comparison of the 3D PF results with the solutions from the axisymmetric model. Solid lines are the saddle point solution from the axisymmetric model based on different anisotropy strength δ. Dotted line marks the critical wavelength λ_c in the isotropic problem. The saddle points in the PF results are given by averaging the two nearest numerical samples where the one with smaller perturbation amplitude recovers and the one with larger amplitude breaks. The error bar in the PF results marks the amplitude of the two nearest samples. On the left-hand-side of the dot line, the scale of the x axis is different from the right-hand-side. (b) Saddle point surface profile from the axisymmetric model for different perturbation wavelengthes with $\delta = 0.3$ (c) Crenellated saddle point wire shapes from the axisymmetric model for different perturbation wavelengthes with $\delta = 0.3$.

$a(z)$ from a uniform wire, one can write

$$R(z) = R_0 + a(z). \tag{26}$$

Given a generalized form of the axisymmetric surface anisotropy near a sidewall facet

$$\tilde{\gamma}(\theta) = \gamma_0 \left[1 + \delta(B_\rho |\cos\theta| + A_\rho |\sin\theta|)\right], \tag{27}$$

where the parameters A_ρ and B_ρ can be determined analytically (as in the case of the $\{100\}$ oriented wires) or by fitting the local surface energy and its first derivative near the sidewall orientation. The Euler-Lagrange equation (Eq.23) can be linearized as the following using the R expansion in Eq.26

$$-\gamma_0 \left(A_\rho \delta + 1\right)\left(\frac{1}{R_0} - \frac{a(z)}{R_0^2}\right) - \frac{\mu_{axi}}{\Omega} + \gamma_0 \frac{d^2 a(z)}{dz^2} = 0, \tag{28}$$

where only leading order terms and $O(a)$ terms are kept. In the derivation, it can be shown that $\tilde{\gamma} - R_z d\tilde{\gamma}/d\theta$ is reduced to $\gamma_0(1 + A_\rho\delta)$ near $\theta = \pi/2$ (see Appendix).

At the leading order, Eq.28 gives the constant volume condition for a uniform wire

$$\frac{\mu_{axi}}{\Omega\gamma_0} = -(1 + A_\rho\delta)/R_0. \tag{29}$$

At the first order in a, Eq.28 is

$$(1 + A_\rho\delta)\frac{a(z)}{R_0^2} + \frac{d^2 a(z)}{dz^2} = 0. \tag{30}$$

Assuming the rough part is going downhill from the upper facet to the lower facet, Eq.30 gives a rough part solution

$$a(z) = \frac{d^*}{2}\cos\left(\pi\frac{z - z_+}{l_r}\right), \tag{31}$$

with z_+ being the z coordinate at the end of the upper facet (see Fig.7), critical modulation amplitude d^* and

$$l_r = \pi R_0/\sqrt{1 + A_\rho\delta}. \tag{32}$$

It is noted that, at this order, the length of the rough part is only

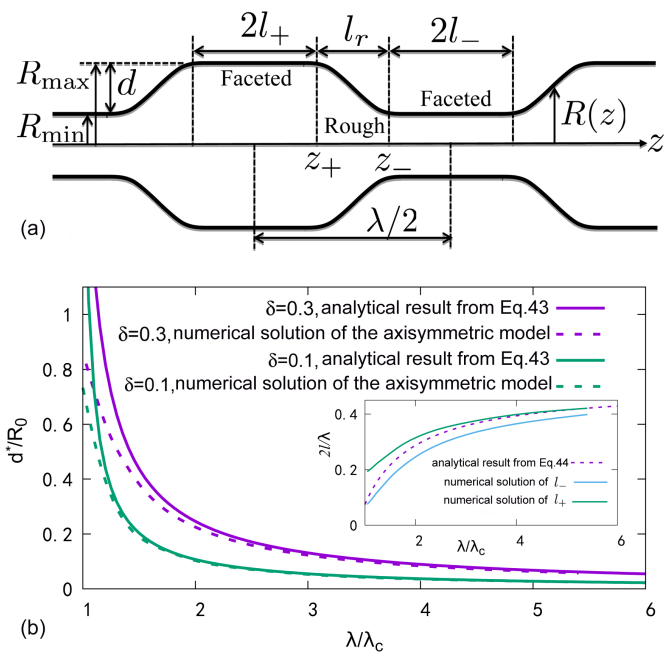

FIG. 7: (a) Schematic plot of the shape-modulated nanowire in the axisymmetric model. The upper facet length is $2l_+$, the lower facet length is $2l_-$, and the length of the connecting rough part which lies between z_+ and z_- is l_r. The modulation amplitude d is $R_{max} - R_{min}$. Distance from the center of the upper facet to the center of the lower facet is a half perturbation wavelength. (b) Comparison of the critical modulation amplitude from the numerics and the analytical theory for the axisymmetric model with $\delta = 0.3$. A comparison of the facet length is also shown in the inset figure.

a function of the wire radius R_0 and the anisotropy parameter $A_\rho\delta$, and does not depend on the perturbation wavelength. However, Eq.32 is obtained from the first order approximation of Eq.23. The full numerical solution of Eq.23 shown in Fig.6b did have a wavelength dependent rough part.

On the facets, from Eq.26 and Eq.31, the wire radii of the upper and the lower facets are given by

$$R = R_0 \pm d^*/2, \tag{33}$$

with $+$ for the upper facet and $-$ for the lower facet. To evaluate the two curvature contributions in the Euler-Lagrange equation (Eq.23) on the facets, we need to calculate the average of each term on the facet part since $d\tilde{\gamma}/d\theta$ is undefined on the facet. On the upper facet, the $\kappa_1(\tilde{\gamma} + d^2\tilde{\gamma}/d\theta^2)$ term is averaged as

$$\begin{aligned}\frac{1}{2l_+}\int_{z_+-2l_+}^{z_+}\left(\tilde{\gamma}+\frac{d^2\tilde{\gamma}}{d\theta^2}\right)\kappa_1 ds &= \frac{1}{2l_+}\int_{\pi/2^+}^{\pi/2^-}\left(\tilde{\gamma}+\frac{d^2\tilde{\gamma}}{d\theta^2}\right)d\theta \\ &= \frac{\gamma_0 B_\rho\delta}{l_+},\end{aligned} \tag{34}$$

with surface element ds. $\pi/2^+$ and $\pi/2^-$ are the local surface orientation at $z_+ - 2l_+$ and z_+. On the lower facet, the same average gives

$$\frac{1}{2l_-}\int_{z_-}^{z_-+2l_-}\left(\tilde{\gamma}+\frac{d^2\tilde{\gamma}}{d\theta^2}\right)\kappa_1 ds = -\frac{\gamma_0 B_\rho\delta}{l_-}, \tag{35}$$

with z_- being the coordinate at the left end of the lower facet. The second term in Eq.23 averages to

$$\frac{1}{2l_+}\int_{z_+-2l_+}^{z_+}\kappa_2\left(\tilde{\gamma}-R_z\frac{d\tilde{\gamma}}{d\theta}\right)ds = -\gamma_0(1+A_\rho\delta)/R, \tag{36}$$

on the upper facet and

$$\frac{1}{2l_-}\int_{z_-}^{z_-+2l_-}\kappa_2\left(\tilde{\gamma}-R_z\frac{d\tilde{\gamma}}{d\theta}\right)ds = -\gamma_0(1+A_\rho\delta)/R, \tag{37}$$

on the lower facet since $R_z = 0$ on the facet.

With Eqs.34 to 37, and the Taylor expansion of $1/R$ using Eq.33, the Euler-Lagrange equation (Eq.23) becomes

$$-\frac{\gamma_0 B_\rho\delta}{l_+} - \frac{\gamma_0}{R_0}(1+A_\rho\delta) + \frac{d^*}{2}\frac{\gamma_0}{R_0^2}(1+A_\rho\delta) - \frac{\mu_{axi}}{\Omega} = 0, \tag{38}$$

on the upper facet and

$$\frac{\gamma_0 B_\rho\delta}{l_-} - \frac{\gamma_0}{R_0}(1+A_\rho\delta) - \frac{d^*}{2}\frac{\gamma_0}{R_0^2}(1+A_\rho\delta) - \frac{\mu_{axi}}{\Omega} = 0, \tag{39}$$

on the lower facet. Since the chemical potential part can be replaced by Eq.29, Eqs.38 and 39 can be further simplified to a single equation

$$B_\rho\frac{\delta}{l_\pm} - \frac{d^*}{2R_0^2}(1+A_\rho\delta) = 0, \tag{40}$$

which indicates that the length of the upper and the lower facets are equal at this order and it is related to the modulation amplitude d^* by

$$l_+ = l_- = l = \frac{2R_0^2 B_\rho\delta}{d^*(1+A_\rho\delta)}. \tag{41}$$

Since $l_+ + l_- + l_r = \lambda/2$, combining Eq.32 and Eq.41 gives

$$\frac{4R_0^2 B_\rho\delta}{d^*(1+A_\rho\delta)} + \frac{\pi R_0}{\sqrt{1+A_\rho\delta}} = \frac{\lambda}{2}, \tag{42}$$

which can be rearranged to give the critical modulation amplitude

$$d^* = \frac{4R_0 B_\rho\delta}{\pi\left(\frac{\lambda}{\lambda_{c0}} - \frac{1}{\sqrt{1+A_\rho\delta}}\right)(1+A_\rho\delta)}. \tag{43}$$

Replacing d^* in Eq.41 gives the facet length

$$l = \frac{\pi R_0}{2}\left(\frac{\lambda}{\lambda_{c0}} - \frac{1}{\sqrt{1+A_\rho\delta}}\right). \quad (44)$$

Eqs.43 and 44 indicate that, in the long wavelength limit ($m = \frac{\lambda}{\lambda_{c0}} >> 1$), the nanowire becomes more sensitive to shape perturbations since the critical modulation amplitude $d^*/R_0 \to 0$. Also, the rough part becomes small in the long wavelength limit since the modulation becomes small and the facet length $l/(m\pi R_0) \to 1/2$.

For the $\{100\}$ oriented nanowire, the arc-length averaged γ (Eq.27) gives $A_\rho = 1$ and $B_\rho = \frac{1+\delta}{\pi/4+\delta}$. In Fig. 7b, comparison of the analytical theory in Eqs.43 and 44 with the exact numerical solutions from the axisymmetric model using the arc-length averaged γ is shown. The critical modulation amplitude d^* is well captured in the theory for perturbations wavelength $\lambda \geq 2\lambda_c$. Also, the identical facet length given in Eq.41 is only a first order approximation. Numerical solutions given in Fig. 7(b) demonstrated that the lengths of the upper and lower facets are different in general. Near λ_c, the modulation amplitude in the analytical result diverges while the numerical solution still gives a finite amplitude. Despite of the axisymmetric approximation we made, the weakly nonlinear analysis reveals a novel finite amplitude stability condition for the $\{100\}$ oriented nanowire which is quantitatively consistent with the PF simulation results.

The weak stabilizing effect in the $\{110\}$ orientated wire can also be explained by the analytical theory above. The numerical study of the γ derivative near the stabilizing cusp as a function of the anisotropy strength parameter δ in Fig.8 reveals that the γ derivative at the plus or the minus side of the sidewall orientation $\theta = \pi/2$ is proportional to δ^2 which can be translated to $B_\rho \sim \delta$ in Eq.27. For $\delta << 1$, Eq.43 gives the small modulation amplitude stability condition observed in the PF simulation.

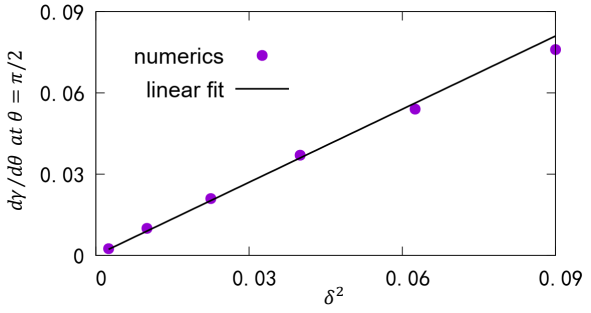

FIG. 8: The γ derivative at the plus side of the sidewall orientation $\pi/2$ as a function of the anisotropy parameter δ from the arc-length averaged γ for $\{110\}$ oriented nanowires.

The length in all the analysis above is scaled by the critical instability wavelength $\lambda_{c0} = 2\pi R_0$ (or the wire radius R_0) of the isotropic Rayleigh-Plateau problem. One can turn the analytical results above into real units with a given wire radius.

DISCUSSION AND CONCLUSIONS

Through simulations and analytics, it is shown that the fragmentation of nanowires may happen by a finite-amplitude non-linear instability mechanism. The PF simulation results can be well explained by the axisymmetric model constructed using arc-length averaged surface energy of the full 3D anisotropy function. Further theoretical analysis of the axisymmetric model of 100 oriented nanowires shows that the critical modulation amplitude of the nanowire surface beyond which the fragmentation may happen can be predicted analytically as a function of the perturbation wavelength, the uniform wire radius, and the parameters in the anisotropic surface energy. The theory also explains the weak stabilization effect of surface facets observed in the 110 oriented nanowire simulations qualitatively. Further quantitative comparison for 110 wires will be left for future studies.

However, the results presented in this paper only give the stability condition of a crystalline wire which is solely decided by the surface configuration. The experimentally observed spacing between nanospheres after the breakup, on the other hand, is typically related to the maximum perturbation growth rate which depends on the dynamical details of atom transport during the process and is not included in our analysis in this paper.

This research was partially supported by Grant No. DE-FG02- 07ER46400 from the U.S. Department of Energy, Office of Basic Energy Sciences. N.W. also acknowledges the support of computer time from GTIIT HPC center.

Regularization of the anisotropic surface energy

The surface energy used in the main text is not smooth since the derivative of γ with respect to the surface orientation angle is not defined on the facet. A small regularization parameter ϵ is used to smooth out the γ near the facets in numerics. For the 3D PF model, a regularized form for the $\{100\}$ oriented nanowire

$$\gamma = \gamma_0\left[1+\delta\left(\sqrt{\epsilon^2+(n_x^0)^2}+\sqrt{\epsilon^2+(n_y^0)^2}+\sqrt{\epsilon^2+(n_z^0)^2}\right)\right], \quad (45)$$

is used. For the axisymmetric model

$$\tilde{\gamma} = \gamma_0\left[1+\delta\left(B_\rho\sqrt{\epsilon^2+\cos^2\theta}+A_\rho\sqrt{\epsilon^2+\sin^2\theta}\right)\right], \quad (46)$$

is used.

To demonstrate this regularization technique in detail, comparison with a previously discussed regularization scheme in Ref.[33] for a simple 2-dimensional (2D) surface energy

$$\gamma(\theta) = \gamma_0[1+\delta(|\sin\theta|+|\cos\theta|)], \quad (47)$$

is made in Fig. 9. Results here should also apply to the regularization formulas (Eqs.45 and 46) used in this work. In the previous work[33], Eq.47 was regularized in a piecewise

fashion by modifying the original γ only when $|\theta - \theta_c| \leq \theta_0$ where θ_c corresponds to the facet orientation, θ_0 is a small regularization range. The regularization method used in this work is

$$\gamma(\theta) = \gamma_0 \left[1 + \delta \left(\sqrt{\epsilon^2 + \sin^2\theta} + \sqrt{\epsilon^2 + \cos^2\theta}\right)\right]. \quad (48)$$

This function is applied globally since the effect of ϵ is only significant close to the facet. As shown in Fig. 9, Eq.48 is a

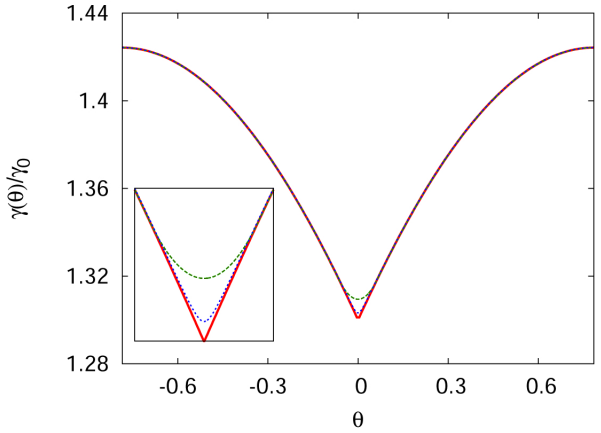

FIG. 9: Comparison of the original 2D γ plot (Eq.47) with its regularized form with $\delta = 0.3$. The inset is a blowup of the cusp region. Solid line: the original anisotropy function with a sharp cusp. Dashed line: the regularized form using ref.[33] method with $\theta_0 = \pi/50$. Dotted line: the regularized form using Eq.48 with ϵ=0.01

fairly good regularization for the original γ in Eq.47.

Newton-Raphson solver for the axisymmetric model

In this section, the Newton-Raphson method used for solving the axisymmetric model in this paper is discussed in detail. However, only the Jacobian matrix for the isotropic problem is shown here. For the anisotropic surface energy model, the Jacobian becomes large and tedious, and will not be written down explicitly here.

The isotropic version of the axisymmetric model is

$$-\gamma\left[-\frac{1}{R\sqrt{1+R_z^2}} + \frac{R_{zz}}{(1+R_z^2)^{3/2}}\right] + \frac{\mu_{axi}}{\Omega} = 0. \quad (49)$$

Linear stability analysis of this equation recovers the classic stability condition $\lambda_c = 2\pi R_0$ with uniform wire radius R_0. To solve Eq.49, we first translate it into a discretized form using finite difference scheme. For each point i along the axial z coordinate, we have an equation

$$\begin{aligned} F_i(\vec{R}) &= \frac{\gamma}{\sqrt{1+\left(\frac{R_{i+1}-R_{i-1}}{2h}\right)^2}} \\ &- \frac{\gamma R_i\left(\frac{R_{i+1}+R_{i-1}-2R_i}{h^2}\right)}{\left[1+\left(\frac{R_{i+1}-R_{i-1}}{2h}\right)^2\right]^{3/2}} + R_i\frac{\mu_{axi}}{\Omega} = 0, \end{aligned} \quad (50)$$

where h is the spatial discretization, $\vec{R}$ is for $R_1, R_2, ..., R_N$, and N is the total number of spatial points. A solution of Eq.49 must satisfy Eq.50 at every grid point. From an initial configuration $\vec{R}^*$, any slightly perturbed configuration can be written as

$$F_i(\vec{R}^* + \delta\vec{R}) \simeq F_i(\vec{R}^*) + \sum_{j=1}^{N} \frac{\partial F_i}{\partial R_j}\Big|_{R=R^*} \delta R_j, \quad (51)$$

using the Taylor expansion. If the new configuration is a solution (i.e. $F_i(\vec{R} + \delta\vec{R}) = 0$), we get a set of N linear equations from Eq.51

$$\sum_{j=1}^{N} \frac{\partial F_i}{\partial R_j}\Big|_{R=R^*} \delta R_j = -F_i(\vec{R}). \quad (52)$$

Or, in the matrix form

$$\mathbf{J} \cdot \delta\vec{R} = -F(\vec{R}), \quad (53)$$

where the Jacobian matrix $J_{ij} = \frac{\partial F_i}{\partial R_j}$. Eq.53 for $\delta\vec{R}$ is solved iteratively using the linear algebra routines from GNU Scientific Library until it converges. To guarantee the convergence of this scheme, one has to start with an initial configuration which is close enough to the solution. Such a configuration can be constructed from the weakly nonlinear approximation discussed in the main text of this paper. To reach solutions with large modulation amplitude where the weakly nonlinear approximation is not good enough to converge the solver, one has to start with small amplitude approximation at long wavelength and reduces the wavelength gradually such that the initial configuration $\vec{R}^*$ for solving the equation set at wavelength λ is good enough to give a solution at wavelength $\lambda + \delta\lambda$.

For the anisotropic surface energy model, the same routine is used to formulate the solver. One only needs to replace Eq.50 with the corresponding anisotropic version.

Anisotropic surface energy for nanowires grown along other orientations

In the simulations of the $\{100\}$ nanowires, the 3 $\{100\}$ orientations coincide with the 3 axes of the cubic simulation box, and the nanowire axial direction is set along the z axis. To simulate a nanowire grown along a different crystal orienta-

tion in the simulation box, one needs to rotate the $\{100\}$ energy anisotropy function such that the nanowire axial orientation in the rotated anisotropy function coincides with the z axis in the simulation box. This procedure is demonstrated in the following derivation of the $\{110\}$ surface anisotropy function.

The anisotropic energy function for the cubic crystal symmetry is

$$\gamma(\hat{n}) = \gamma_0 \left[1 + \delta(|n^{100}| + |n^{010}| + |n^{001}|)\right]. \quad (54)$$

For a $\{100\}$ oriented nanowire, this anisotropy function has to be re-written using simulation box coordinates

$$\gamma(\hat{n}^0) = \gamma_0 \left[1 + \delta(|n_x^0| + |n_y^0| + |n_z^0|)\right], \quad (55)$$

where the surface normal components on the crystal surface are replaced by the components n_x^0, n_y^0, n_z^0 in the simulation box coordinate since the 3 crystal axes are aligned with the 3 simulation box coordinates.

For a $\{110\}$ oriented nanowire, one needs to rotate the $\{110\}$ crystal axis in Eq.54 and align it with the z axis in the simulation box. A $\pi/4$ rotation around the original x axis is needed. A standard vector rotation yields

$$n_x^r = \frac{n_x^0}{\sqrt{2}} - \frac{n_z^0}{\sqrt{2}}, \quad (56)$$

$$n_y^r = n_y^0, \quad (57)$$

$$n_z^r = \frac{n_x^0}{\sqrt{2}} + \frac{n_z^0}{\sqrt{2}}, \quad (58)$$

from which one can write the anisotropy function for the $\{110\}$ nanowire as

$$\gamma_{\{110\}}(\hat{n}) = \gamma_0 \left[1 + \delta(|n_x^r| + |n_y^r| + |n_z^r|)\right]. \quad (59)$$

approximation of $\tilde{\gamma} - R_z \frac{d\tilde{\gamma}}{d\theta}$

In the axisymmetric model, the arc-length averaged surface energy is

$$\tilde{\gamma}(\theta) = \gamma_0 \left[1 + \delta(B_\rho |\cos\theta| + A_\rho |\sin\theta|)\right]. \quad (60)$$

Near the sidewall orientation $\theta_0 = \pi/2$, it can be expanded as

$$\tilde{\gamma} \simeq \gamma_0 (1 + A_\rho \delta) + \frac{d\tilde{\gamma}}{d\theta}\Big|_{\pi/2} (\theta - \frac{\pi}{2}). \quad (61)$$

Near $\theta_0 = \pi/2$, R_z is

$$R_z = -cot\theta \simeq -cot\frac{\pi}{2} + csc^2\frac{\pi}{2}(\theta - \frac{\pi}{2}) = \theta - \frac{\pi}{2}, \quad (62)$$

$d\tilde{\gamma}/d\theta$ is

$$\frac{d\tilde{\gamma}}{d\theta} \simeq \frac{d\tilde{\gamma}}{d\theta}\Big|_{\pi/2} + \frac{d^2\tilde{\gamma}}{d\theta^2}\Big|_{\pi/2} (\theta - \frac{\pi}{2}). \quad (63)$$

Using the 3 expressions above one has

$$\tilde{\gamma} - R_z \frac{d\tilde{\gamma}}{d\theta} \simeq \gamma_0 (1 + A_\rho \delta) - \frac{d^2\tilde{\gamma}}{d\theta^2}\Big|_{\pi/2} (\theta - \frac{\pi}{2})^2. \quad (64)$$

The last term in the above expression can then be ignored.

[1] S. Karim, M. E. Toimil Molares, A. G. Balogh, W. Ensinger, T. W. Cornelius, E. U. Khan, and R. Neumann, Nanotechnology **17**, 5954-5959 (2006).

[2] S. Karim, M. E. Toimil Molares, W. Ensinger, A. G. Balogh, T. W. Cornelius, E. U. Khan, and R. Neumann, J. Phys. D: Appl. Phys. **40**, 3767-3770 (2007).

[3] F. M. Kolb, H. Hofmeister, M. Zacharias and U. Gösele, Appl. Phys. A **80**, 1405-1408 (2005).

[4] X. H. Huang, Z. Y. Zhang, X. Wang, Z. Zhang, G. Z. Xing, D. L. Guo, D. P. Leusink, L. X. Zheng, and T. Wu, Appl. Phys. Lett. **97**, 203112 (2010).

[5] C. P. Hsiung, H. W. Liao, J. Y. Gan, T. B. Wu, J. C. Hwang, F. Chen, and M. J. Tsai, Acs Nano **4**, 5414 (2010).

[6] Simon Vigonski and Ville Jansson and Sergei Vlassov and Boris Polyakov and Ekaterina Baibuz and Sven Oras and Alvo Aabloo and Flyura Djurabekova and Vahur Zadin, Nanotechnology **29**, 015704 (2018).

[7] Tao Wan, Ying Pan, Haiwei Du, Bo Qu, Jiabao Yi, and Dewei Chu, ACS Appl. Mater. Interfaces 10, 3, 2716 (2018).

[8] A. I. Hochbaum, R. Chen, R. D. Delgado, W Liang, E. C. Garnett, M Najarian, A. Majumdar and P. Yang, Nature **451**, 163 (2008).

[9] P. M. Wu, J. Gooth, X. Zianni, S. F. Svensson, J. G. Gluschke, K. A. Dick, C. Thelander, K. Nielsch, and H. Linke, Nano Lett. **13**, 4080 (2013).

[10] J. Plateau, Transl. Annual Reports of Smithsonian Institution, p. 1863-1866 (1873).

[11] Lord Rayleigh, Proc. London. Math. Soc. **10**, 4-13 (1878).

[12] K. F. Gurski and G. B. McFadden, Proc. R. Soc. Lond. A **459**, 2575-2598 (2003).

[13] K. F. Gurski and G. B. McFadden, SIAM. J. Appl. Math. **66**, No.4, 1163-1187 (2006).

[14] J. W. Cahn., Scr. Metall **13**, 1069 (1979).

[15] J. S. Stölken and A. M. Glaeser, Scr. Metal. **27**, 449-454 (1992).

[16] W. C. Carter and A. M. Glaeser, Mater. Sci. Eng. **89**, L41 (1987).

[17] Q. Ma, Acta. Mater. **46**, 1669 (1998).

[18] L. Kulinsky, J. D. Powers and A. M. Glaeser, Acta. Mater. **44**, 4115 (1996).

[19] A. M. Glaeser, Interface. Sci. **9**, 65-82 (2001).

[20] M. K. Santala, and A. M. Glaeser, Acta. Mater. **56**, 1967-1980 (2008).

[21] W. J. Boettinger, W, A, Warren, C. Beckermann and A. Karma, Annu. Rev. Mater. Res. **32**, 163 (2002).

[22] D. Tourret, H. Liu, J. LLorca, Progress in Materials Science **123**, 100810 (2022).

[23] Long-Qing Chen, Yuhong Zhao, Progress in Materials Science **124**, 100868 (2022).

[24] A. Kumar, B. Bourdin, G. A. Francfort, O. Lopez-Pamies, J. Mech. Phys. Solids **142**, 104027 (2020).
[25] J. J. Wang, B. Wang, L. Q. Chen, Annu. Rev. Mater. Res. **49**, 127 (2019).
[26] Y. Gu, N. Wang, F. Xue, L.Q. Chen, Phys. Rev. B **91**, 174103 (2015).
[27] Kehao Zhang, Simin Feng, Junjie Wang, Angelica Azcatl, Ning Lu, Rafik Addou, Nan Wang, Chanjing Zhou, Jordan Lerach, Vincent Bojan, Moon J Kim, Long-Qing Chen, Robert M Wallace, Mauricio Terrones, Jun Zhu, Joshua A Robinson, Nano. Lett. **15**, 6586 (2015).
[28] S. Fashu, J. Yang, L. Yang, N. Wang, The European Physical Journal E **43**, 1-7 (2020).
[29] N. Moelans, B. Blanpain, P. Wollants, Phys. Rev. B **78**, 024113 (2008).
[30] N. Wang, Y. Wen, L.Q. Chen, Philo. Mag. Lett. **94**, 794-802 (2014).
[31] Nan Wang, Moneesh Upmanyu, and Alain Karma, Phys. Rev. Materials **2**, 033402 (2018).
[32] N. Wang and N. Provatas, Phys. Rev. Applied **7**, 024032 (2017).
[33] J. Debierre, A. Karma, F. Celestini, and R. Guerin. Phys. Rev. E **68**, 041604 (2003).